

1 **Gravity wave induced instability of the stratospheric polar vortex edge**

2 Lawrence Coy,^{a,b} Paul A. Newman,^a William M. Putman,^a Steven Pawson,^a and
3 M. Joan Alexander^c

4 ^a*NASA GSFC, Greenbelt, MD, USA*

5 ^b*SSAI, Lanham, MD, USA*

6 ^c*NWRA, Boulder, CO, USA*

7 *Corresponding author:* Lawrence Coy, lawrence.coy@nasa.gov

8 ABSTRACT: We report on a previously undocumented process capable of mixing Northern Hemi-
9 sphere (NH) winter Ertel potential vorticity (EPV)—instabilities introduced along the stratospheric
10 polar vortex edge by breaking gravity waves (GWs). As horizontal resolution has increased, global
11 scale atmospheric models and data assimilation systems (DAS) are now able to capture some
12 aspects of GW generation, propagation, and dissipation, as well as mesoscale EPV disturbances.
13 This work examines resolved GWs, their breaking, and their interaction with the stratospheric polar
14 vortex as seen in the NASA Global Modeling and Assimilation Office DAS during the 2021–2022
15 NH winter. This analysis shows that tropospheric generated GWs, breaking in the stratosphere
16 over a substantial area, created a significant disruption of the polar vortex EPV, in turn trigger-
17 ing baroclinic instabilities near the edge of the polar vortex. The instabilities take the form of
18 mesoscale vortices propagating on the edge of the stratospheric polar vortex. This work reveals
19 two new features in the EPV analysis: high and low fluctuations at the smallest model scale created
20 by resolved GW breaking, and high values associated with mesoscale vortices along the edge of
21 the polar vortex.

22 SIGNIFICANCE STATEMENT: The northern hemisphere (NH) winter stratospheric polar vor-
23 tex is typically disturbed by global scale waves that displace, distort, and weaken the vortex,
24 however, as the resolution of global models has increased, the role played by smaller scale waves in
25 disturbing the stratospheric vortex can now be evaluated. As one example, the NH winter of 2022
26 had unusually weak global scale waves along with strong smaller scale waves generated by flow
27 over mountains, providing an ~~idea~~-ideal case for evaluating the effects brought about by the smaller
28 scale waves. Our examination of the 2022 NH winter reveals that the waves generated by flow over
29 mountains, located under the stratospheric vortex, propagated up to the middle stratosphere where
30 they broke down, interfering significantly with the vortex flow. This distortion of the vortex flow
31 created an unstable region that led to the formation of “mesoscale vortices”, relatively small eddies
32 on the edge of the polar vortex, that then propagated coherently around the stratospheric vortex.
33 The importance of these, small scale wave generated, mesoscale vortices may lie in their potential
34 to mix trace gases across the stratospheric vortex boundary.

35 **1. Introduction**

36 Past studies of the stratosphere have emphasized the importance of Ertel’s potential vorticity
37 (EPV) as a well conserved dynamical tracer (Hoskins et al. 1985). These early studies often
38 dealt with limited horizontal resolution making the identification of important global EPV features
39 remarkable at the time. For Example, McIntyre and Palmer (1983) characterized the EPV fields
40 used in their discovery of breaking planetary waves as “. . . resembling a blurred view of reality seen
41 through a pane of knobby glass . . .”. This “knobby glass” has been smoothed considerably over
42 the following decades based on data assimilation techniques in conjunction with high horizontal
43 resolution global models. Indeed, recent data assimilation reanalysis of the McIntyre and Palmer
44 (1983) breaking wave examples provides dynamically consistent confirmations of their breaking
45 planetary wave discovery (Butchart 2022).

46 While the planetary scale waves are well resolved in modern EPV fields, the question arises
47 as to the possibility of increased model resolution leading to new discoveries. That is, can
48 “magnification” of current EPV fields provide further insights into stratosphere and mesosphere
49 dynamics. Here we investigate two new features resulting from increased horizontal resolution:

50 signatures of breaking gravity waves (GW) followed by the formation of mesoscale vortices on the
51 polar vortex edge.

52 The Northern Hemisphere (NH) stratospheric polar vortex forms every winter, however, consid-
53 erable vortex variability exists, especially in years with stratospheric sudden warmings (SSWs).
54 During SSW events, high ~~Ertel potential vorticity (EPV)~~ EPV in the stratospheric polar vortex is
55 mixed down to lower latitudes by global-scale planetary waves. The planetary waves are said to
56 be “breaking” when they create regions where the latitudinal EPV gradient is reversed and these
57 reversed gradient regions can lead to instabilities in the wave breaking region (see Butchart 2022,
58 and references therein).

59 Here we report on another process capable of mixing NH winter EPV—instabilities introduced
60 along the polar vortex edge by breaking gravity waves (GW). GWs are generated by flow over
61 orography, convection, fronts, or flow instabilities (Alexander 2010). Their successful vertical
62 propagation depends on the background atmospheric flow. Under the right conditions GWs can
63 transfer significant momentum and energy from the troposphere to the middle atmosphere. As
64 vertically propagating GWs encounter lower densities or approach a critical layer, they increase in
65 amplitude until they become unstable and “break” “break”, depositing momentum and energy to
66 the background flow and hence providing the possibility of disrupting the winter stratospheric polar
67 vortex. Parameterizations of this GW momentum drag attempt to capture these effects, playing a
68 major role in the upper stratosphere momentum budget and a significant role in some SSW events
69 (Albers and Birner 2014; Achatz et al. 2024).

70 As noted above, global scale atmospheric models and data assimilation systems (DAS)
71 routinely resolve the main features of the stratospheric polar vortex along with planetary wave
72 variability and breaking. As the horizontal resolution has increased over time these models
73 are now able to capture convective systems and some aspects of GW generation, propagation,
74 and dissipation (Holt et al. 2017; Stevens et al. 2019; Shibuya and Sato 2019; Okui et al. 2023)
75 (Watanabe and Miyahara 2009; Holt et al. 2017; Stevens et al. 2019; Shibuya and Sato 2019; Okui et al. 2023)
76 . Here we report on resolved GWs, their breaking, and their interaction with the stratospheric
77 polar vortex as seen in the NASA Global Modeling and Assimilation Office (GMAO) near real
78 time forward processing (FP) system during the 2021–2022 NH winter.

79 Our plan is to examine a somewhat atypical NH winter (2021–2022), where planetary wave
80 activity was relatively weak and the stratospheric polar vortex strong, allowing GWs to dominate
81 the polar vortex disturbances. The working hypothesis is that orographically generated GWs,
82 breaking in the mid-to upper stratosphere, distorted the edge of the polar vortex, creating regions
83 of unstable EPV gradients. These in turn generated a series of what will be called here mesoscale
84 vortices, incorporating signatures of latitudinal mixing, on the edge of the polar vortex.

85 The process of longitudinally localized GWs acting to generate larger-scale,
86 planetary waves has been observed and modeled in the mesosphere
87 (Smith 1996; Siskind et al. 2010; Matthias and Ern 2018; Sato et al. 2018). These studies
88 demonstrate the ability of GWs to make significant changes at larger scales. Here we extend these
89 studies to examine the role of GWs in the creation of mesoscale vortices near the edge of the
90 stratospheric polar vortex using a high horizontal resolution data assimilation system.

91 As will be shown below, the mesoscale vortices generated by the breaking ~~gravity waves~~ GWs
92 developed centers with extremely high EPV. While EPV is often well conserved in the stratosphere
93 (Haynes and McIntyre 1990), diabatic and frictional forces can change the EPV of an air parcel
94 (Haynes and McIntyre 1987) and such non-conservation processes must be occurring here. The
95 development and propagation of the high EPV mesoscale vortices will be documented below,
96 however, a detailed EPV budget is left for future studies.

97 In the following, Section 2 provides a description of the DA systems and models used. The
98 main DAS is the NASA GEOS (Global Earth Observing System) FP system, however some lower
99 horizontal resolution MERRA-2 (Modern-Era Retrospective analysis for Research and Applica-
100 tions) output is included for comparison. To investigate the potential for baroclinic instability near
101 the polar vortex edge, results are presented from a linear quasi-geostrophic beta plane model, also
102 described in Section 2. The results are presented in Section 3, with subsections on the 2021-2022
103 NH winter, the resolved GWs, the structure of the mesoscale vortices, dependence on resolution,
104 and the linear instability model. A summary of the results along with conclusions are presented in
105 Section 4.

2. Global Assimilation Products and Data

a. GEOS FP System

The NASA GMAO GEOS FP DAS routinely produces global, near-real-time, meteorological analysis fields and forecasts available at three hourly intervals. This system updates frequently (approximately every six months) to better incorporate new data types and the latest model developments. The DAS utilizes a full suite of observation types including aerosol, temperature, pressure, radiances, winds, moisture, radio occultation, and ozone measurements. Each six hourly analysis assimilates roughly two million observations. Zhu et al. (2022) provides a current description of the GEOS DAS.

The system used during the NH winter of 2021–2022 was run at ~ 12 km horizontal resolution on a cubed sphere grid (Putman and Lin 2007) with meteorological fields saved on a $5/16$ by $1/4$ degree longitude by latitude horizontal grid and on either the full 72 model levels (model top at 0.01 hPa) or vertically interpolated to 42 pressure levels. A description of the model physics can be found in Arnold et al. (2020). The most recent two weeks of forecasts are available on the NASA Center for Climate Simulation (NCCS) data portal. The specific archived analysis fields used in the study are available as described in the Open Research Section.

Taking the horizontal grid resolution for GEOS FP as ~ 12.5 – 14 km and the system’s effective resolution as $\sim 7\times$ the grid resolution, yields ~ 87.5 – 98 km as the effective system resolution. The width of the Scandinavian ridge is about 300 km while the gravity waves resolved waves examined below have a horizontal scale of ~ 300 – 500 km, both well within the effective resolution of GEOS FP.

To investigate the dependence on horizontal resolution, EPV fields are shown from a test DAS (x0048) run at half the GEOS FP system resolution (24 km). While the GEOS FP ($\sim 1/8$ degree) and the test system ($\sim 1/4$ degree) are run with different horizontal resolutions, the results are saved on the same output grid. Note that the MERRA-2 system ($\sim 1/2$ degree), described below, is also included in the resolution comparisons.

b. MERRA-2

The MERRA-2 system provides ongoing global atmospheric reanalyses starting in 1980. Unlike the FP system, the MERRA-2 system is frozen, with only the input data changing with time. The

135 MERRA-2 vertical levels are the same as in FP, however MERRA-2, with fields saved at 5/8 by
 136 1/2 degree longitude by latitude, has more coarse horizontal resolution than FP. An overview of
 137 MERRA-2 is given by Gelaro et al. (2017). Here we used the monthly averaged pressure level
 138 fields (GMAO 2015b) when comparing the NH winter 2022 climate with other winters and the
 139 instantaneous model level EPV fields (GMAO 2015a) when comparing specific time EPV fields
 140 between FP and MERRA-2.

141 *c. Linear Instability Model*

142 The potential for baroclinic instability near the disturbed vortex edge is investigated using a
 143 quasi-geostrophic, beta-plane, linear instability model. This is the same model used and described
 144 in McCormack et al. (2014) and is based on the adiabatic and frictionless, linearized potential
 145 vorticity equation (see Andrews et al. 1987, equation 3.4.5 and following equations):

$$q'_t + \bar{u}q'_x + v'\bar{q}_y = 0. \quad (1)$$

146 where q is [quasi-geostrophic](#) potential vorticity, u and v are the longitudinal and meridional velocity
 147 components, and x , y , t , are the longitudinal and meridional directions and time. The overbars
 148 denote a zonal average and the primes the deviation from a zonal average. Since q' and v' depend
 149 linearly on the geostrophic stream function, ψ , assuming a wave solution for ψ with phase speed
 150 c and zonal wavenumber k allows the x and t derivatives to be evaluated. With \bar{u} and \bar{q}_y then
 151 specified as the environment to be tested for instability, and suitable boundary conditions, Eq. 1
 152 can be finite differenced for a chosen value of k as:

$$\mathbf{A}\psi = c\mathbf{B}\psi \quad (2)$$

153 where the matrix, \mathbf{A} , depends on \bar{u} and \bar{q}_y , the matrix, \mathbf{B} , depends on the Laplacian operator, and
 154 ψ is the vector of stream function values at each point in the two dimensional, latitude and altitude,
 155 domain being investigated.

156 Eq. 2, can be solved for ψ and c , using standard routines. For simplicity we assume that the
 157 instability is located far enough from the latitude and altitude domain boundaries that we can take ψ

158 equal to zero on all boundaries. Examination of the imaginary part of c allows for the identification
159 of the fastest growing mode structure, ψ , for each value of k specified.

160 *d. AIRS data*

161 For confirmation of the DAS resolved GWs we examined the GW signature found in the AIRS
162 (Atmospheric Infrared Sounder on the NASA Aqua satellite) $4.3 \mu\text{m}$ brightness temperature signal.
163 Horizontal resolution is 13.5 km at the nadir point below the satellite, similar to the resolution
164 of the FP system, and resolution decreases toward the measurement swath edges so that the
165 average resolution is ~ 20 km. The data are low-noise multi-channel averages with weighting
166 functions that peak between 30–40 km altitude (Hoffmann et al. 2014). Brightness temperature
167 wave anomalies are attenuated relative to sensible temperature anomalies, with attenuation that
168 is inversely proportional to vertical wavelength. These channels are most sensitive to the longer
169 vertical wavelength (≥ 15 km) GWs and are not expected to highlight wave breaking regions where
170 the vertical wavelength decreases. Note also that selected AIRS channels are assimilated in the
171 DAS so that the AIRS observations shown here are not entirely independent of the data assimilation
172 output, nevertheless, the AIRS observations shown here can be regarded as an independent analysis
173 of the GWs in the FP system forecasts.

174 **3. Results**

175 *a. The 2021–2022 Northern Hemisphere Winter Stratosphere*

176 The zonal mean of the zonal wind component at 10 hPa, 60°N provides a useful measure of
177 polar vortex strength that can be used to characterize the NH winter stratosphere. Winters with
178 high seasonally averaged DJF (December, January, February) winds either lack SSWs or have them
179 occurring late in the winter season. The 2021–2022 NH winter had the largest mean seasonal wind
180 seen in the 1980–2023 MERRA-2 time period, with a mean seasonal wind of 46.3 ms^{-1} , more than
181 1.5 standard deviations above the average value of 30.3 ms^{-1} .

182 As with the winds, the planetary-scale wave forcing from the troposphere can be considered over
183 the DJF season and variability is expected depending on interannual tropospheric variability. Here
184 we consider the zonally averaged meridional heat flux at 100 hPa and 60°N as a measure of the wave
185 forcing of the stratosphere. The NH 2021–2022 winter season had the lowest meridional heat flux

186 seen in the 1980-2023 MERRA-2 time period, with a mean seasonal heat flux of 17.2 Kms^{-1} , more
187 than 2 standard deviations below the average value of 24.3 Kms^{-1} . The record low 2021–2022
188 planetary-scale wave forcing at 100 hPa and 60°N is consistent with the strong stratospheric winds.

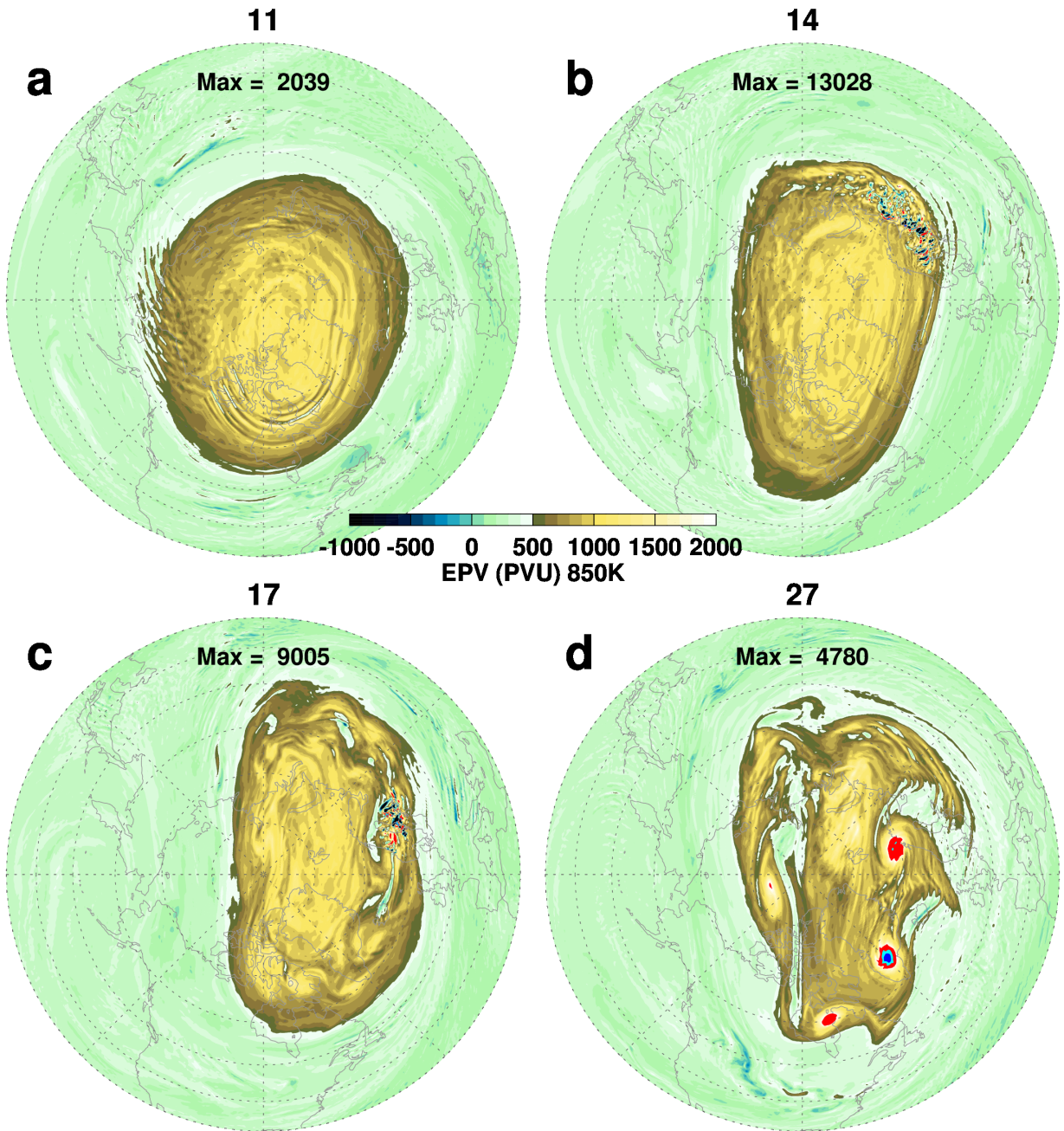
189 The strong winds and low wave forcing conjure up a picture of an undisturbed zonally symmetric
190 polar vortex. Nevertheless, the January 2022 stratospheric polar vortex transformed from a zonally
191 symmetric high Ertel potential vorticity (EPV) configuration (Fig. 1a) on 11 January to a much
192 more disturbed vortex (Fig. 1d) on 27 January. While there is an overall elongation of the 27 January
193 high EPV region, the most striking features are the ragged edge of the vortex (the high EPV region)
194 and the existence of four very high, localized EPV mesoscale vortices along the polar vortex edge.
195 On 11 January the maximum 850K EPV was $\sim 2,000 \text{ PVU}$ while by 27 January the maximum had
196 more than doubled to $4,780 \text{ PVU}$ with the highest values associated with the strong EPV mesoscale
197 vortex at 45°W .

202 *b. Resolved gravity waves*

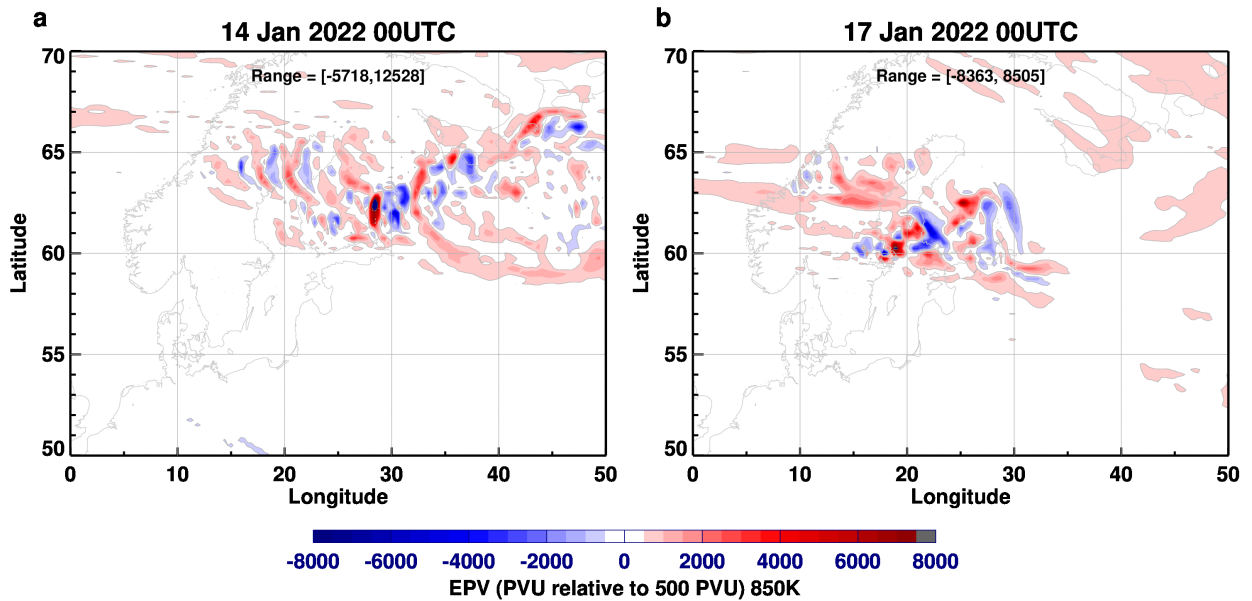
203 Between 11 and 27 January 2022 small regions of extremely high and low EPV values occurred
204 along the vortex edge, especially over Northern Europe with a maximum value of over $13,000 \text{ PVU}$
205 on 14 January (Fig. 1b). The polar vortex edge distorted in response to these perturbations, creating
206 separation of the high EPV from the main vortex on 14 January from 0° – 135°E . By 17 January,
207 the vortex edge became even more distorted as the high and low EPV perturbations continued
208 occurring over Northern Europe (Fig. 1c).

209 Looking more closely at the 850K EPV on 14 and 17 January (Fig. 2), alternating regions of
210 high and low EPV are seen near the polar vortex edge. The EPV values at these times are as much
211 as $8,000 \text{ PVU}$ below and $12,500 \text{ PVU}$ above the polar vortex edge value. On the 14th (Fig. 2a) a
212 high EPV feature is seen equatorward and then east of the disturbance region corresponding to the
213 EPV filament identified in Fig. 1b.

217 That these small-scale EPV disturbances are related to resolved GWs can be seen in the undu-
218 lations in the height of the 850K potential temperature surface (Fig. 3). The GWs in the height
219 field do not disturb the entire EPV field, as non-dissipating GWs should not be visible in the EPV
220 field, however, the EPV field is disturbed in the more northern part of the GW field where the GWs
221 are likely breaking in a non-EPV conserving manner. Note that the EPV varies on a smaller scale



198 FIG. 1. EPV on the 850K potential temperature surface for a) 11, b) 14, c) 17 and d) 27 January 2022 in
 199 potential vorticity units (PVU) where one PVU is equal to $10^{-6}m^2s^{-1}Kkg^{-1}$. The high EPV values are: red:
 200 2000–3000 PVU, cyan: 3000–4000 PVU, blue: 4000–5000 PVU, and yellow: above 5000 PVU. The vortex edge
 201 on 11 January 2022 is located at 500 PVU based on the method of Nash et al. (1996).

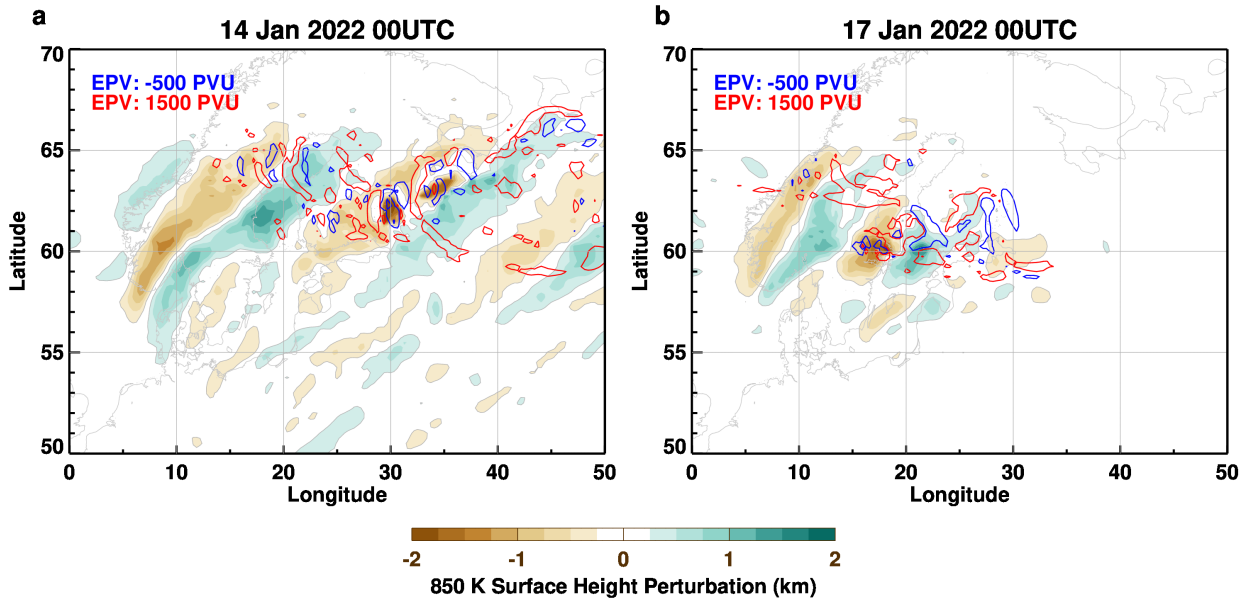


214 FIG. 2. Latitude (50-70°N) longitude (0°-50°E) projection of EPV on the 850K potential temperature surface
 215 for a) 14 January 2022 and b) 17 January 2022. The EPV contours are relative to 500 PVU, the value defining
 216 the vortex edge on 11 January 2022.

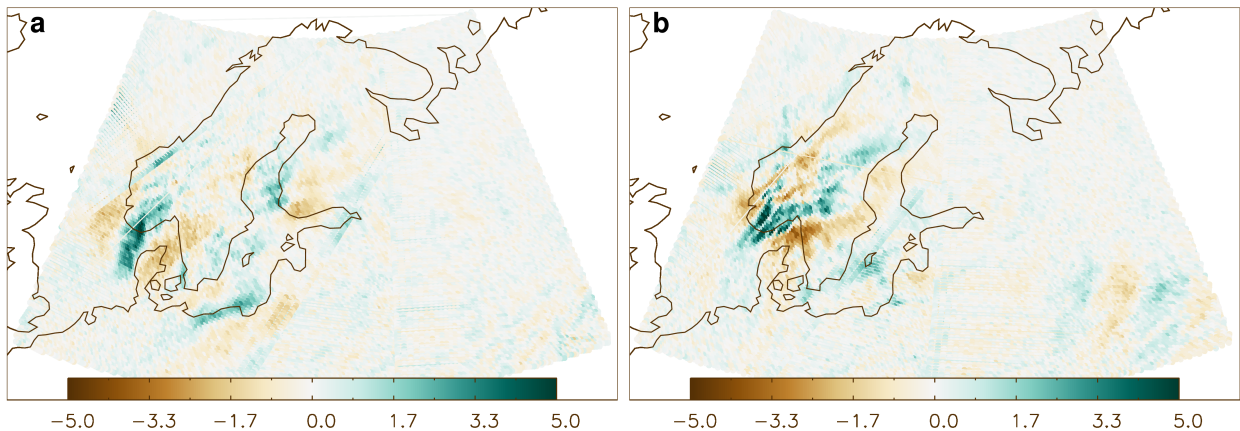
222 than the scale of the GWs seen in the potential temperature surface oscillations and furthermore
 223 that the orientation of the EPV oscillations differs from the orientation of the GWs. This relation
 224 between the GW signature and the scale and orientation of the small-scale EPV field is consistent
 225 with [detailed-3D shear instability](#) model studies of GW breaking and with GW observations (Fritts
 226 and Alexander 2003, and references therein).

230 These model resolved GWs can also be seen directly in the AIRS observations (Fig. 4). These
 231 wave patterns highlight regions over southern Scandinavia where the strong GWs have the largest
 232 vertical wavelengths. Note that these brightness temperatures correspond well with the regions
 233 of potential temperature height surface variations shown in Fig. 3. In the regions where EPV
 234 fluctuations are large the AIRS GW signal is weak. This is more evidence that the EPV fluctuations
 235 characterize regions where GWs are breaking and hence have small vertical wavelengths there.

240 The vertical cross sections of potential temperature and zonal wind on 14 and 17 January (Fig. 5)
 241 highlight the stratospheric breaking wave region, topped by the strong easterly vertical wind shear
 242 and reversal of the zonal wind direction near the stratopause that inhibits the vertical propagation
 243 of orographic GWs. Thus the GWs are required to break in the stratosphere at this time. On both

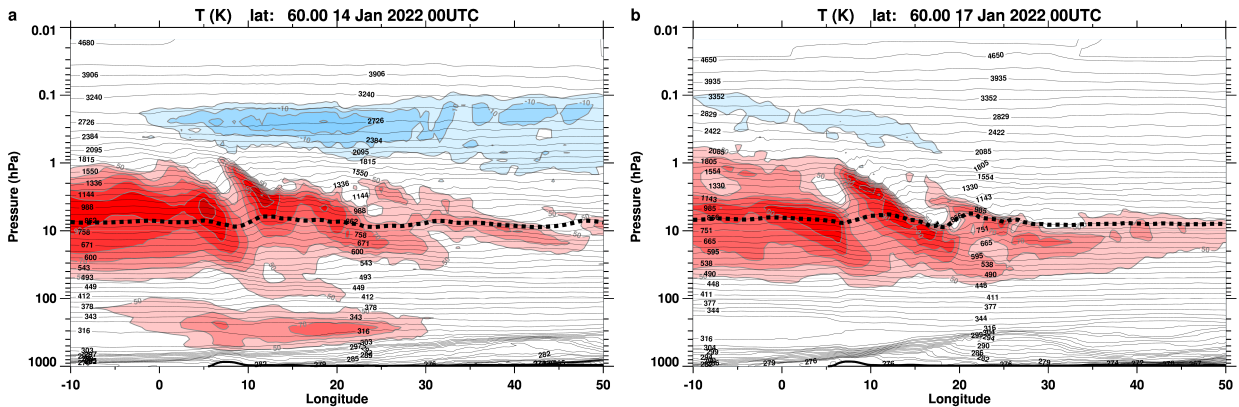


227 FIG. 3. Latitude (50-70°N) longitude (0°W-50°E) projection of the height of the 850K potential temperature
 228 surface (filled contours) and the -500 (blue) and 1500 (red) PVU contours on a) 14 January 2022 and b) 17
 229 January 2022.



236 FIG. 4. AIRS 4.3 μm brightness temperature anomalies on descending (nighttime) overpasses on a) 14 January
 237 and b) 17 January showing large amplitude mountain waves over southern Scandinavia. The UT times listed
 238 are the overpass times that cover the mountain waves. These are low-noise multi-channel averages described in
 239 Hoffmann et al. (2014) with weighting functions that peak between 30-40 km altitude.

244 the 14th and the 17th the strong stratospheric westerlies at 10°W are reduced after crossing the
 245 GW region and are much weaker by at 50°E, ~~an indication that the wave breaking may be reducing~~



251 FIG. 5. Longitude (10°W–50°E) altitude (1000–0.01 hPa) cross section at 60°N of potential temperature (gray
 252 contours) and zonal wind (filled contours). The dotted black curve denotes the 850K potential temperature
 253 surface. The contour interval for the zonal field is 10 ms⁻¹ and only winds great than 50 ms⁻¹ (red shades) and
 254 less than 0 ms⁻¹ (blue shades) are shown.

246 the zonal wind than at 10°W, qualitatively consistent with an expected reduction of the zonal wind
 247 created by breaking GWs in the upper stratosphere. Nearly vertical potential temperature surfaces
 248 are also found on both the 14th and 17th (Fig. 5) indicating breaking gravity waves at 60°N and
 249 likely at nearby latitudes as well, including the 60–65°N regions of small scale EPV features seen
 250 in Fig. 3.

255 These relatively large amplitude GWs in the stratosphere were generated by strong tropospheric
 256 northwesterly winds over Scandinavia (Fig. 6). The synoptic weather situation at this time was
 257 ideal for GW generation with a large, upper-air, high pressure system just west of the European
 258 orography. The westerly wind component in both the troposphere and stratosphere allowed wave
 259 propagation into the upper stratosphere.

260 While the 60°N zonal wind during 2021–22 was relatively strong, it did weaken during January
 261 2022, especially over the breaking gravity wave region (Fig. 7a). This weakening of the zonal wind
 262 after 11 January corresponds to the time of the peak vertical momentum flux over Europe (Fig. 7b).
 263 These strong vertical momentum fluxes are characteristic of GWs. Note that this momentum flux
 264 is greatest in the upper stratosphere and weakens above 1 hPa in the mesosphere, consistent with
 265 the GW wave structure shown in Fig. 5. While the zonal wind changes and peak momentum fluxes
 266 line up closely, the largest GW flux peak occurs about two days after the winds begin to decrease

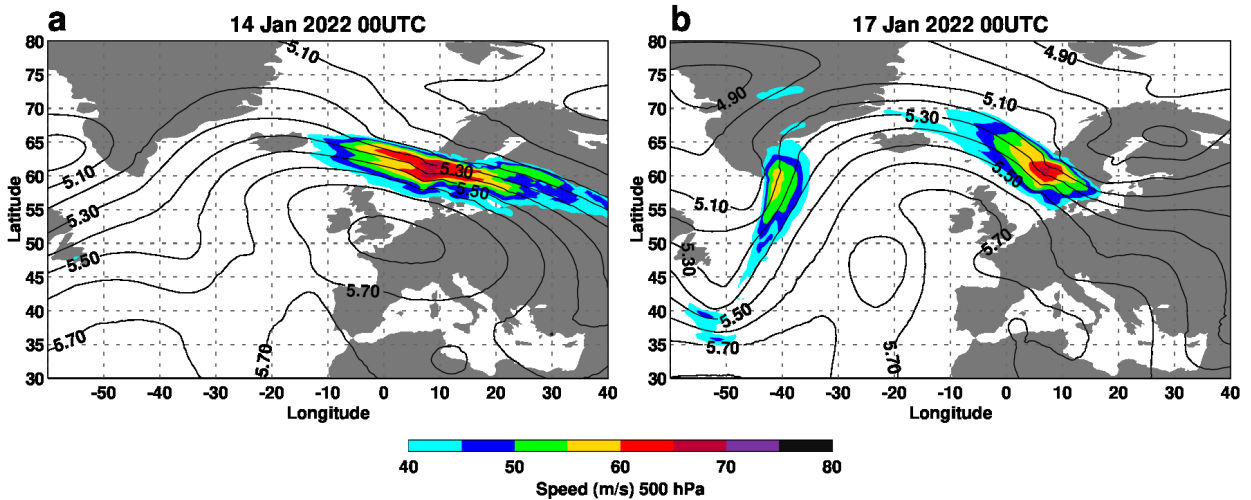
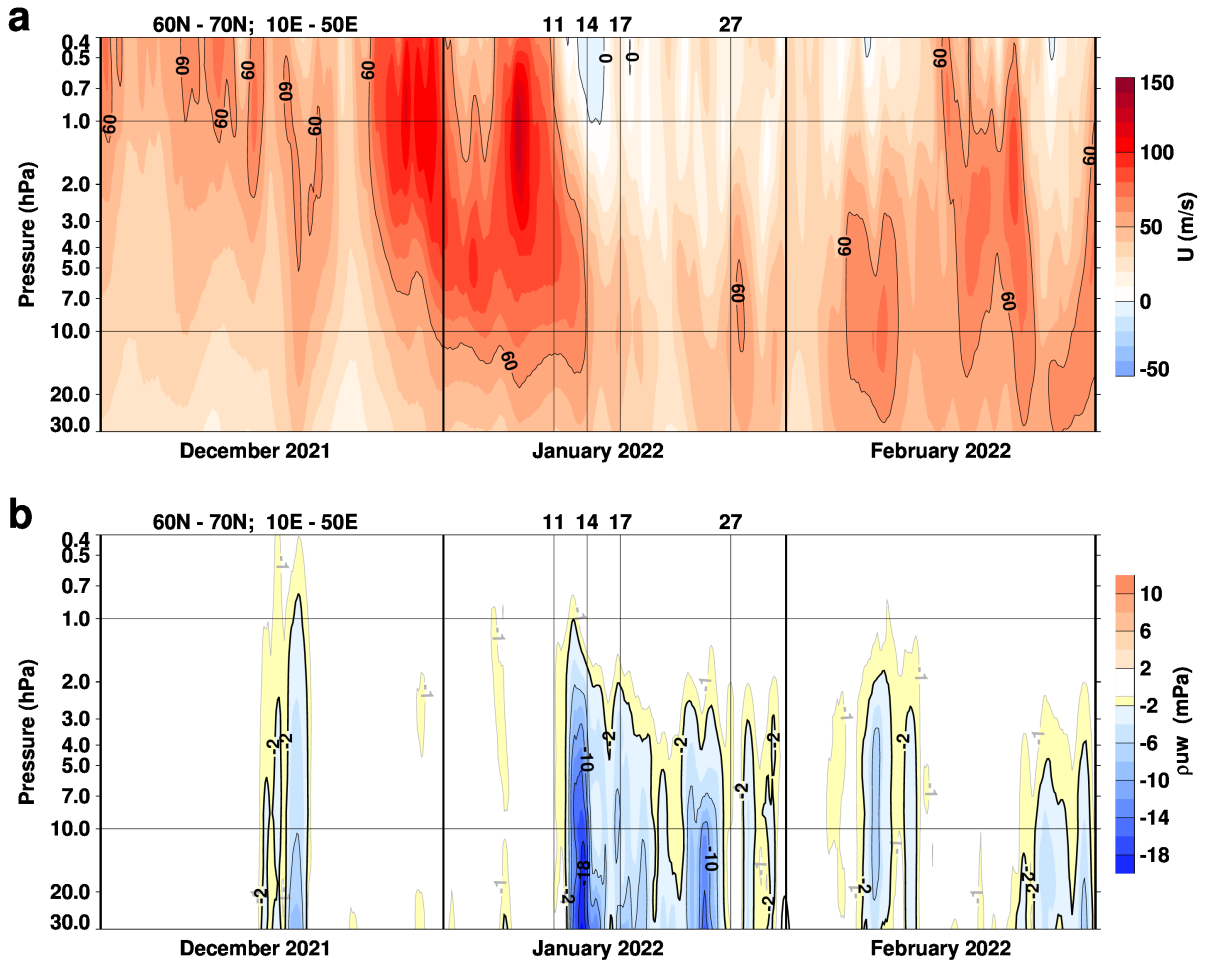


FIG. 6. Wind speed and geopotential heights at 500 hPa for a) 14 January 2022 and b) 17 January 2022.

267 indicating that other factors in the zonal momentum budget, including planetary wave activity
 268 would be needed for a complete momentum budget.

273 The small scale GWs and mesoscale vortices as seen in Fig. 1d can be identified by the occurrence
 274 of high values of enstrophy, the square of the vorticity (Fig. 8a). There is a January 2022 burst of
 275 enstrophy coincident with the strong vertical momentum flux and these upper stratospheric strong
 276 enstrophy values continue to the end of January created by both continued GW activity and the
 277 development of the mesoscale vortices. The $\sim 1/2$ degree horizontal resolution MERRA-2 system
 278 lacks the higher ($\sim 1/8$ degree) horizontal resolution of the NRT-GEOS FP system, hence the small
 279 scale features seen in the NRT-GEOS FP system's enstrophy (Fig. 8a) are not seen in MERRA-2
 280 (Fig. 8b). MERRA-2 captures some of the mesoscale vortices as seen by the slightly high than
 281 average enstrophy values during the last third of January at 10 hPa, however, it misses the very
 282 strong enstrophy values characteristic of GW breaking near mid-January.

285 Note that the identification of breaking GW regions with small-scale, large positive and negative
 286 EPV fluctuations, does not imply that these are being realistically modeled as the scale of the
 287 fluctuations is near the limit of the model resolution. Rather they are taken here as a signature of
 288 GW breaking. Much higher vertical and horizontal resolution simulations are needed to accurately
 289 model the GW breaking process and its effect on EPV. Note that, while both MERRA-2 and
 290 GEOS-FP incorporate orographic GW parameterization (McFarlane 1987), these parameterized



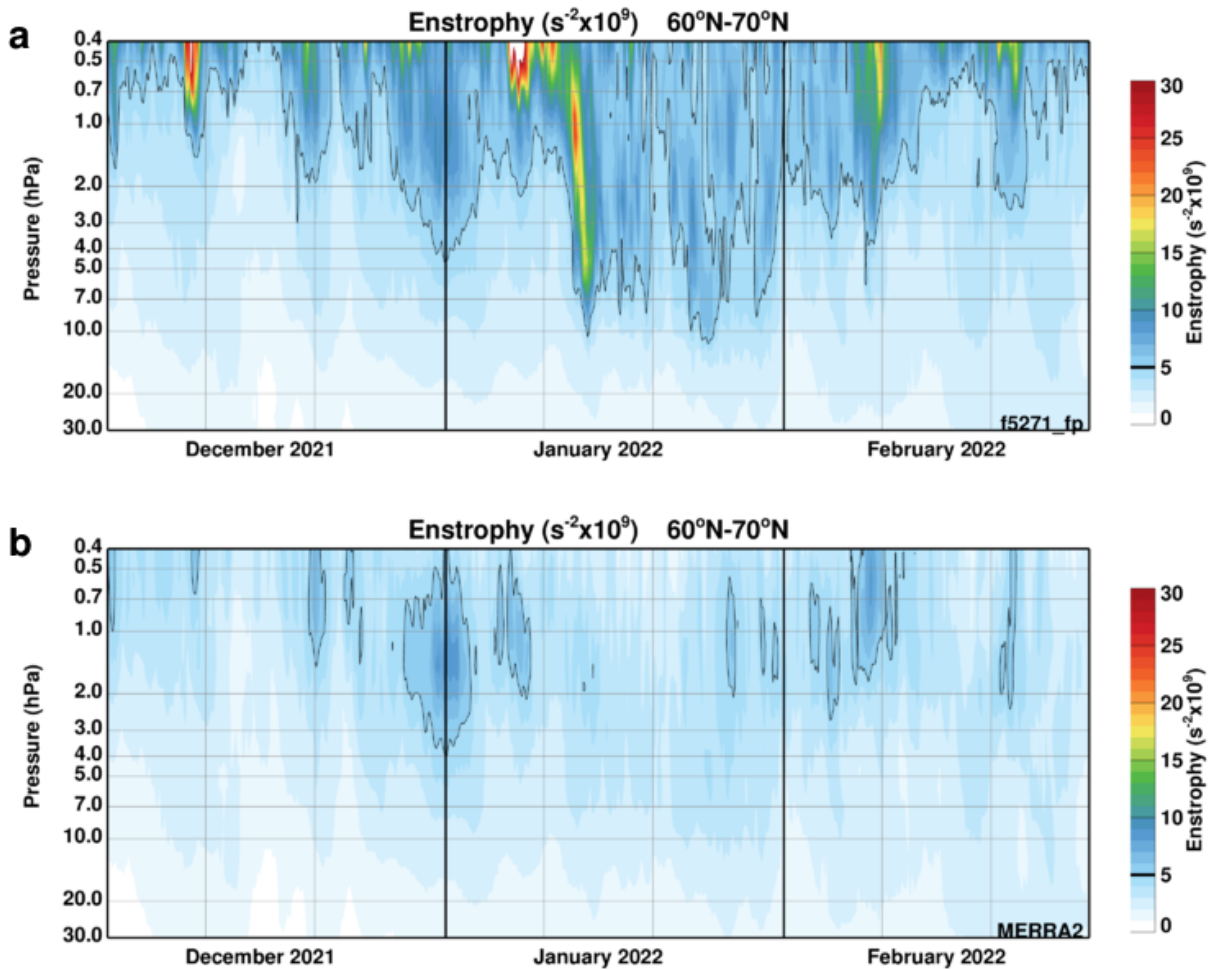
269 FIG. 7. Time (DJF) pressure (30–10 hPa) cross sections averaged over 60°–70°N and 10°–50°E for a) zonal
 270 mean zonal wind (ms^{-1}) and b) the zonal component of the density weighted vertical momentum flux (mPa).
 271 Note that in b) the dark contour is at -2 mPa, not zero, and that the the -1 mPa contour has been added (filled
 272 yellow).

291 GW drag effects remained localized over the orography at an altitude just above the wind maximum
 292 but below the main resolved breaking region.

293 c. Mesoscale vortices

294 d. *mesoscale-Vortices*

295 The mesoscale vortices develop and propagate along the edge of the vortex, just poleward of the
 296 edge value delineating the low and high EPV regions. They begin to form by 14 January 2022



283 FIG. 8. Time (DJF) pressure (30–10 hPa) zonal averages of enstrophy ($s^{-2} \times 10^6$) over 60–70°N for a) the
 284 GMAO-NRT-GEOS-FP system and b) MERRA-2.

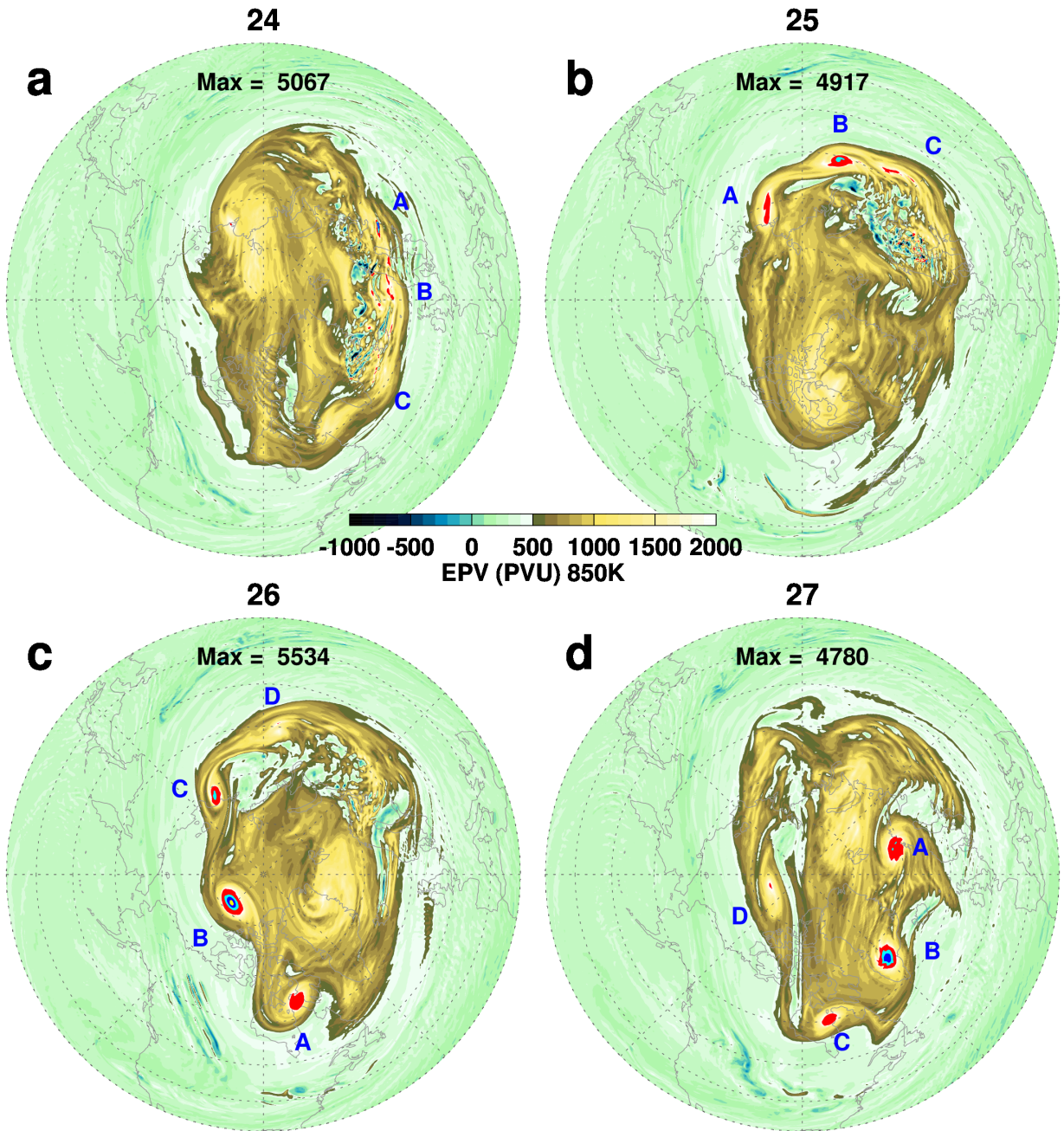
297 when the EPV begins to separate from the vortex (Figs. 1b and c) and continue to develop and
 298 propagate around the vortex throughout the rest of the month. An example of the growth and
 299 propagation of the mesoscale vortices from 24–27 January is shown in figure 9.

300 EPV undulations, identified by the letters, A, B, and C can be seen on 24 January (Fig. 9a) in a
 301 region of EPV that has separated from the main high EPV region by gravity wave breaking (EPV
 302 fluctuations at the smallest resolvable scale) from Greenland to Northern Europe. Note that that
 303 these three EPV undulations can be tracked back at in time at least once around the vortex before
 304 experiencing the growth shown here after 24 January. By 25 January (Fig. 9b), the three mesoscale
 305 vortices have propagated about 90° in longitude around the main vortex. After crossing the main

306 breaking GW region the mesoscale vortices have increased in amplitude, moving in response to the
307 larger EPV values of the polar vortex. The mesoscale vortices, A, B, and C continue to increase in
308 amplitude (the value of their central EPV) on the 26 January (Fig. 9c) and there is also at this time
309 the identification of an additional trailing EPV region labeled D. On the last day shown, 27 January
310 (Fig. 9d), the mesoscale vortices continue their eastward propagation with A and D increasing in
311 amplitude while B and C decrease slightly in amplitude. Note that some of the mesoscale vortices
312 are associated with “breaking wave” signatures in the EPV field: A in panel c), and A, B, and C,
313 in panel d). In each of these mesoscale vortices EPV from the main vortex is being pulled off and
314 lower EPV mixed into the main vortex.

318 The trajectory of the mesoscale vortex B carried it nearly twice around the main vortex (Fig. 10).
319 After ~ 2 days increasing in strength (24–26 January), mesoscale vortex B kept its amplitude nearly
320 constant until ~ 28 January before weakening and crossing over the North Pole on 29 January and
321 eventually dissipating near Northern Europe. Mesoscale vortex B existed for about seven days
322 making its average period for a circulation around the globe approximately three and half days,
323 implying a propagation speed of 45 ms^{-1} at 70°N . This speed is close to the mean polar vortex
324 speed at this time, indicating that mesoscale vortex B has a well-conserved EPV structure during
325 this time.

331 Cross sections of mesoscale vortex B on 26 January highlight typical vertical structure of the
332 mesoscale vortices during their largest amplitude (Fig. 11). The EPV anomaly extends from ~ 10 –
333 1.5 hPa in the upper stratosphere while the potential temperature shows large perturbations starting
334 just above 20 hPa and extending through the upper stratosphere. The temperature perturbation field
335 is consistent with the potential temperature field with cool air below and warm air above. The wind
336 anomalies are located south and north of the axis of the temperature perturbation consistent with
337 the cyclonic circulation of the EPV anomalies. The strongest wind gradients (in the horizontal)
338 coincide with the strongest temperature gradients (in the vertical) [consistent with the thermal wind](#)
339 [relation](#). The wind change across the mesoscale vortex is $\sim 80 \text{ ms}^{-1}$. The mesoscale vortices are
340 located in the upper stratosphere with little extent into the lower stratosphere.

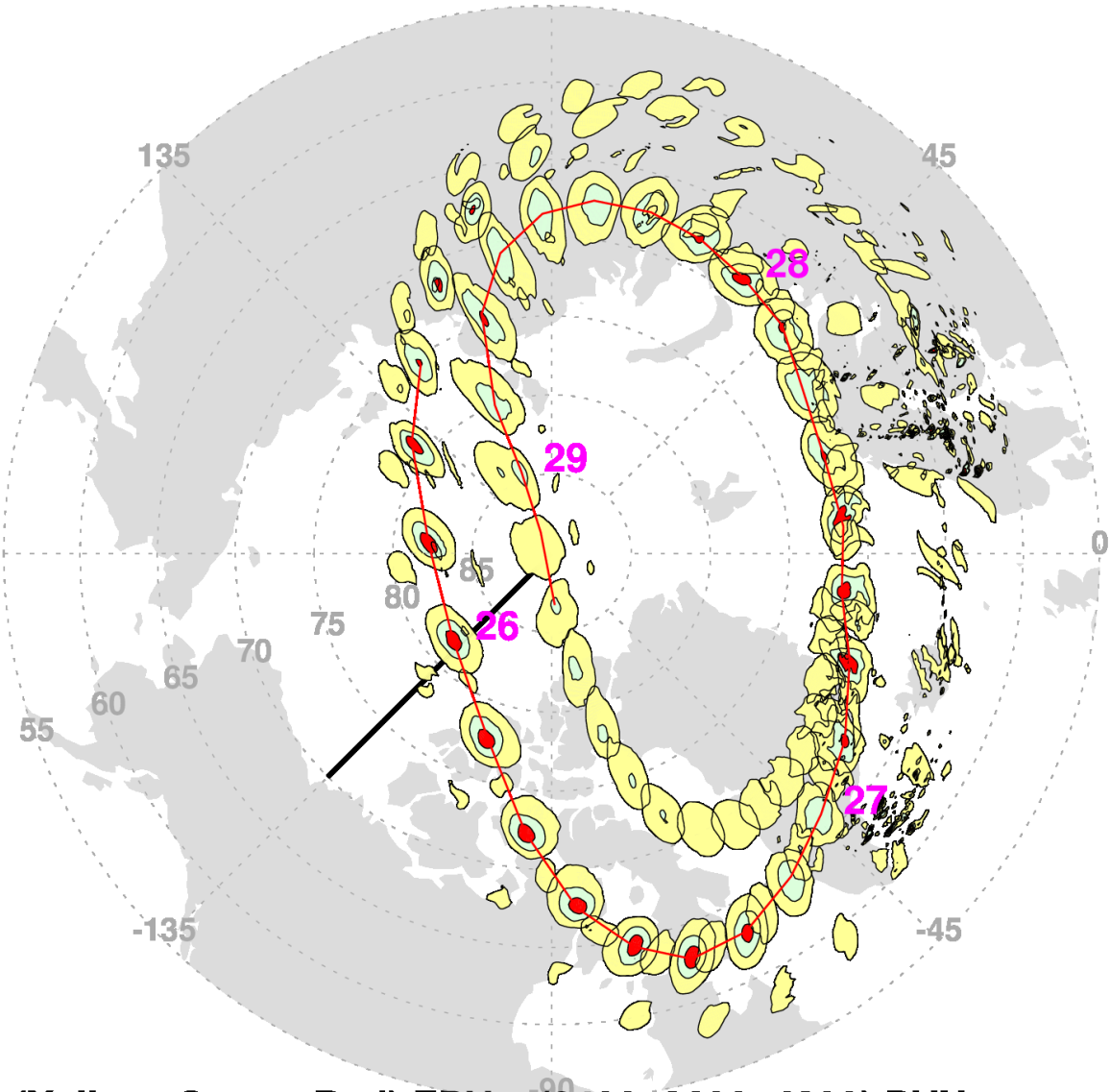


315 FIG. 9. EPV on 850K potential temperature surface for a) 24, b) 25, c) 26, and d) 27 January 2002 00UTC.
 316 The high EPV values are: red: 2000–3000 PVU, cyan: 3000–4000 PVU, blue: 4000–5000 PVU, and yellow:
 317 above 5000 PVU. Features tracked across panels are labeled A, B, C, and D.

345 *d. Resolution*

346 High horizontal resolution is needed to identify the breaking GW signature and to reveal the
 347 detailed structure of the mesoscale vortices. Figure 12 shows the 850 K potential temperature

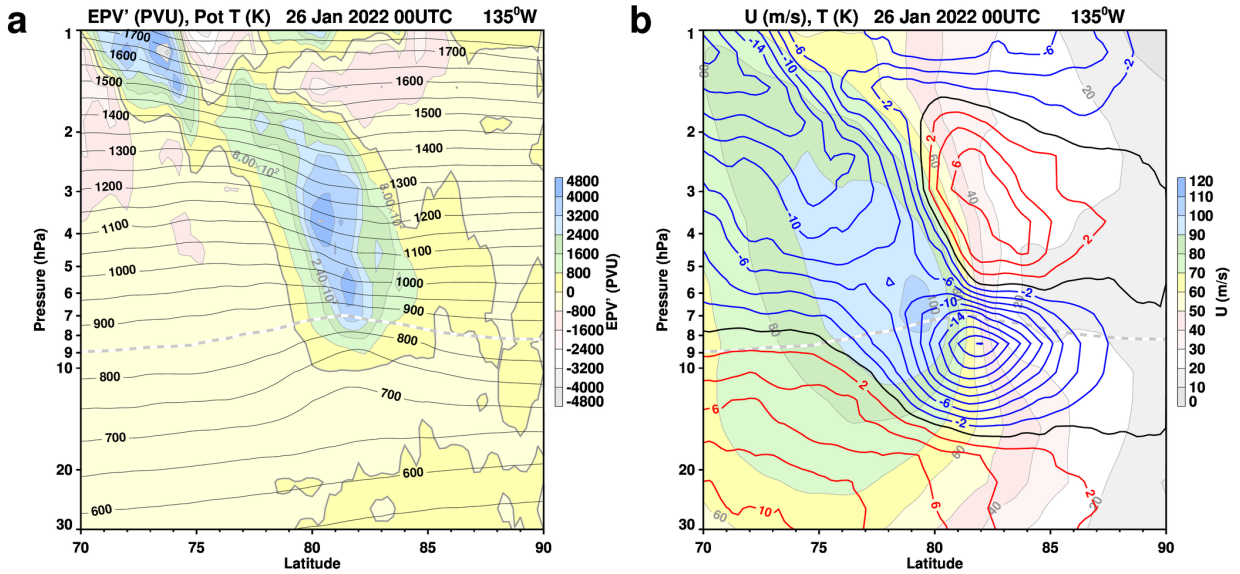
EPV 850K 24-31 Jan 2022



(Yellow, Green, Red) EPV > (2400, 3600, 4800) PVU

326 FIG. 10. EPV on the 850K potential temperature surface for 24–31 January 2022 contoured every three hours.
327 EPV values are colored between 2400–3600 PVU (yellow), 3600–4800 PVU (green), and greater than 4800 PVU
328 (red). The red curve connects the maximum EPV locations from 25 January 15 UTC to 29 January 6 UTC. The
329 locations of the highest EPV at 0 UTC on 26, 27, 28, and 29 January are marked. The black line denotes the
330 location of the cross section shown in Fig. 11.

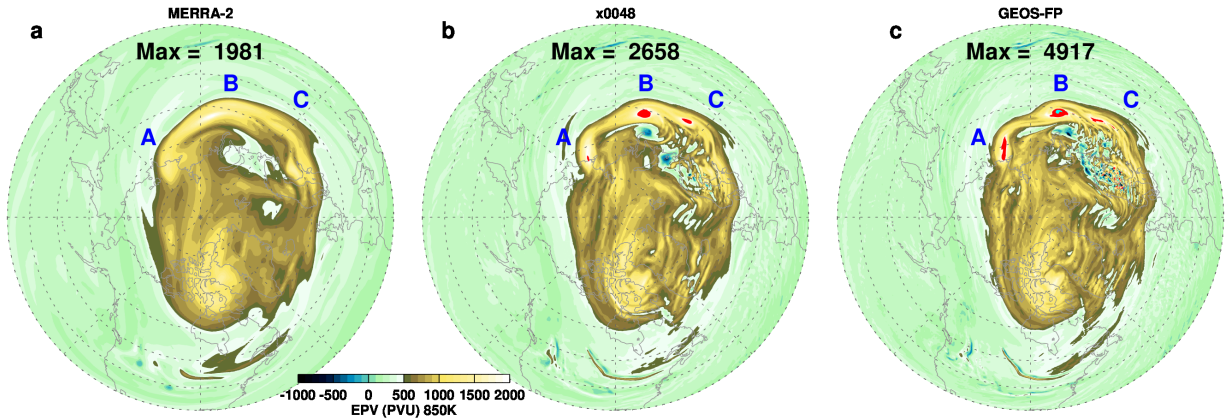
348 surface EPV field at $\sim 1/2$, $1/4$, and $1/8$ degree resolution (low, intermediate, and high). At the
349 lowest resolution, there is no evidence of breaking GWs and while there is some appearance of the



341 FIG. 11. Latitude (70° – 90° N) pressure (30–1 hPa) cross section at 135° W of a) EPV deviation from the
 342 zonal mean (PVU, filled contours) and potential temperature (K, black contours) and b) zonal wind (ms^{-1} , filled
 343 contours) and temperature deviation from the zonal mean (K, red positive, blue negative). The dashed gray curve
 344 denotes the 850K potential temperature.

350 EPV fluctuations at the intermediate resolution, they are much more evident at the high resolution.
 351 The well-defined mesoscale vortices only appear at the intermediate and high resolution and have
 352 the highest central EPV values at high resolution. All three resolutions, even the lowest, capture
 353 the strong EPV region near A, B, and C, separated from the main vortex, creating a reversal in the
 354 latitudinal EPV gradient.

358 Later, on the 27th, the mesoscale vortices have propagated along the main vortex edge as
 359 identified by the letters (Fig. 13). They are very faint but present at low resolution, however both
 360 the intermediate and high resolutions agree well suggesting that the size of mesoscale vortices are
 361 converging with resolution and may not change much in even higher resolution systems. While
 362 the overall structure of the mesoscale vortices are similar at intermediate and high resolution, the
 363 central peak EPV values are still larger at the high resolution. Note that the maximum EPV values,
 364 occurring at mesoscale vortex “B”, increase from 3,014 at intermediate to 4,780 PVU at high
 365 resolution.



355 FIG. 12. EPV on 850K potential temperature surface for GEOS DAS analyses at three horizontal resolutions
 356 with nominal values of a) 1/2, b) 1/4, and c) 1/8 degrees on 25 January 2022 00UTC. Contours are the same as
 357 in Fig. 9

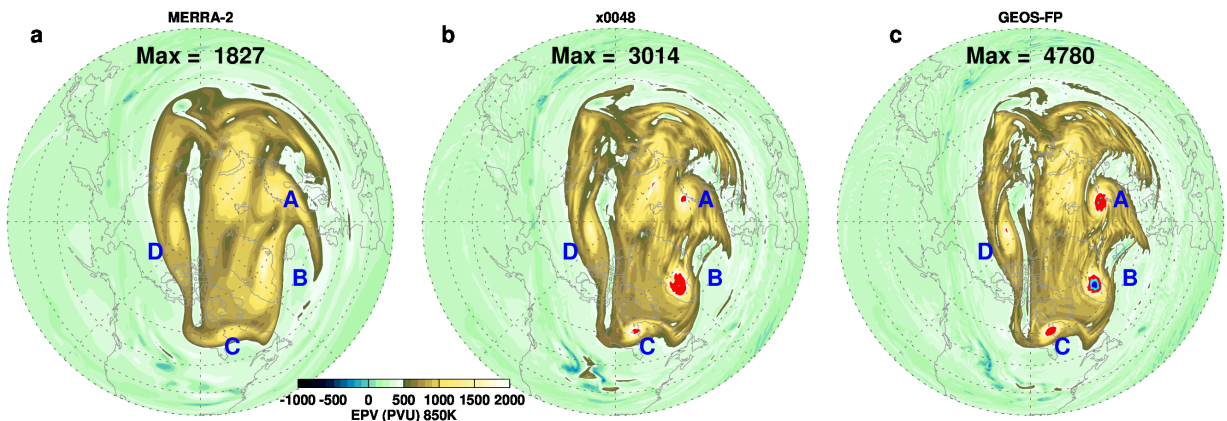


FIG. 13. Same as Fig. 12 but for 27 January 2022 00UTC

366 *e. Instability Considerations*

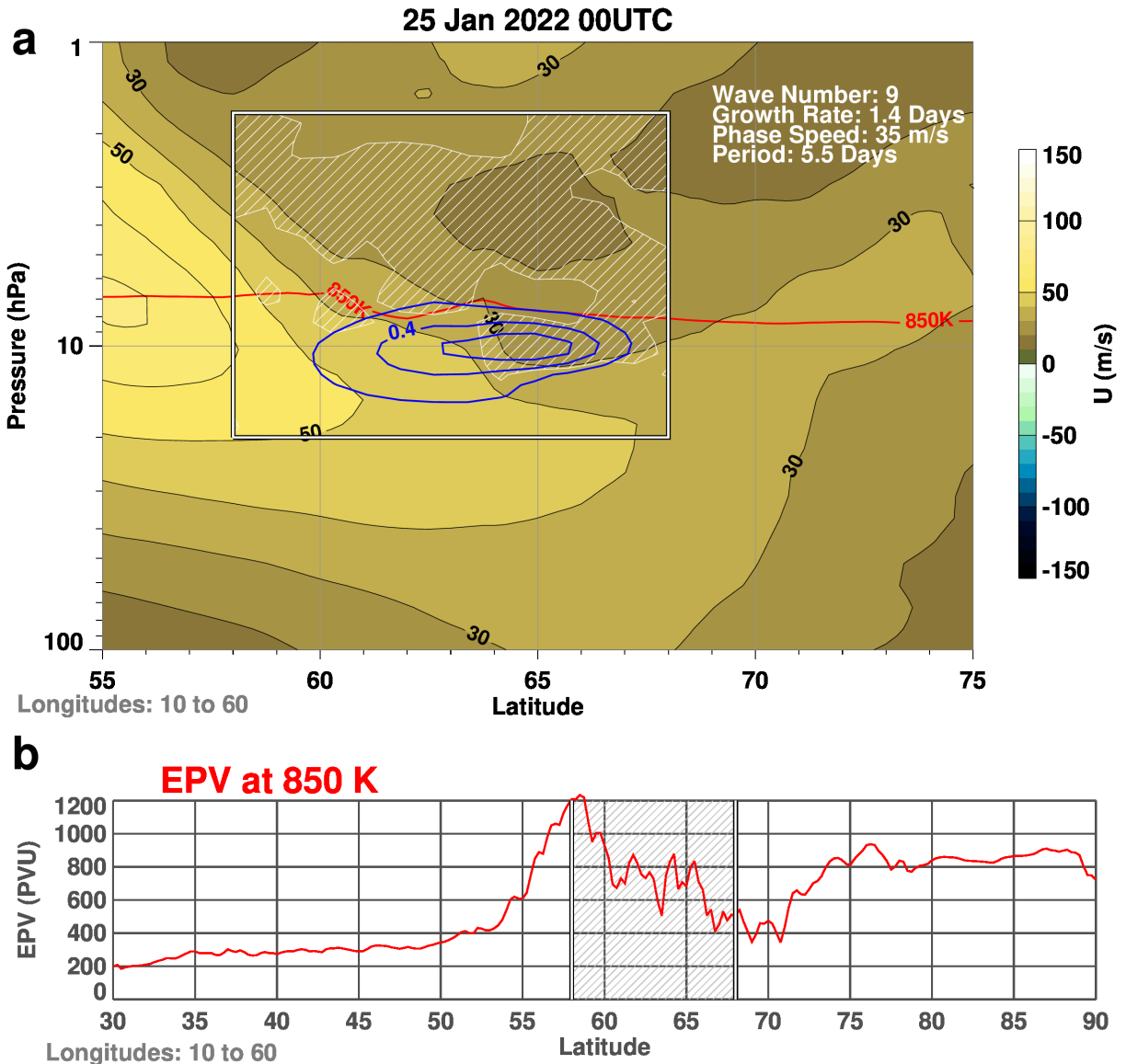
367 The formation of the mesoscale vortices from the smaller scale gravity waves presents a challenge.
 368 One possible mechanism, suggested by the reverse EPV latitudinal gradient over a substantial area,
 369 is that the mesoscale vortices are initially generated by baroclinic instability. The idea presented
 370 here is that the tropospheric generated GWs break in the stratosphere over a substantial area,
 371 creating a significant disruption of the polar vortex EPV, in turn triggering instabilities near the
 372 edge of the polar vortex. The instability then produces the mesoscale vortices. As a simple test of
 373 the instability of the flow, a linear instability model was ~~examine~~ examined for different zonal wind
 374 profiles and times. One result is shown in figure 14. Since the reversed EPV gradient is localized,

375 the zonal winds near the GW activity, 10° – 60° E, were average for the background state. The time
376 chosen was for 25 January as the wave perturbation, especially the perturbations labeled C and D
377 in figure 9, were still growing at that time. Other choices include time averaging of the zonal winds
378 or selecting a different longitude range. In addition the model evaluates instability over a limited
379 latitude and pressure range, here chosen to be 58° – 68° N and 20–2 hPa. As in McCormack et al.
380 (2014) the boundary conditions were simply taken to be zero at all boundaries of the box. The
381 interior of the box includes a region of negative \bar{q}_y (Fig. 14a) and a reversal of the EPV gradient
382 (Fig. 14b).

383 For the above choices the fastest growing unstable wave was found at wavenumber 9, with an
384 e-folding growth rate of 1.4 days, a phase speed of 35 ms^{-1} , and a period of 5.5 days. Examining the
385 spacing of the mesoscale vortex locations of 25 January (Fig. 9b), the wavenumber 9 result is not
386 unrealistic, however the spacing between the mesoscale vortices does increase with time (Fig. 9d)
387 suggesting a smaller wavenumber. The growth rate is reasonable, however the phase speed appears
388 to be somewhat slow, leading to a period that is longer than observed when compared to the just
389 over 3-day circuit of the globe taken by the mesoscale vortex B (Fig. 9) from 26–29 January
390 (Fig. 10). The amplitude structure is confined to the lower region of the model’s domain in contrast
391 to the larger vertical extent seen in figure 11. Overall, the instability model results, while not
392 comprehensive, illustrate the potential for instability created by the breaking GW induced reversal
393 in the local EPV latitudinal gradient.

394 Note that this instability model cannot ~~reproduced~~ reproduce the observed growth in EPV as no
395 diabatic processes are included. In the this simple model, the EPV is rearranged to correspond
396 to the growing amplitude wave. The finite amplitude behavior of the instability requires a more
397 sophisticated model.

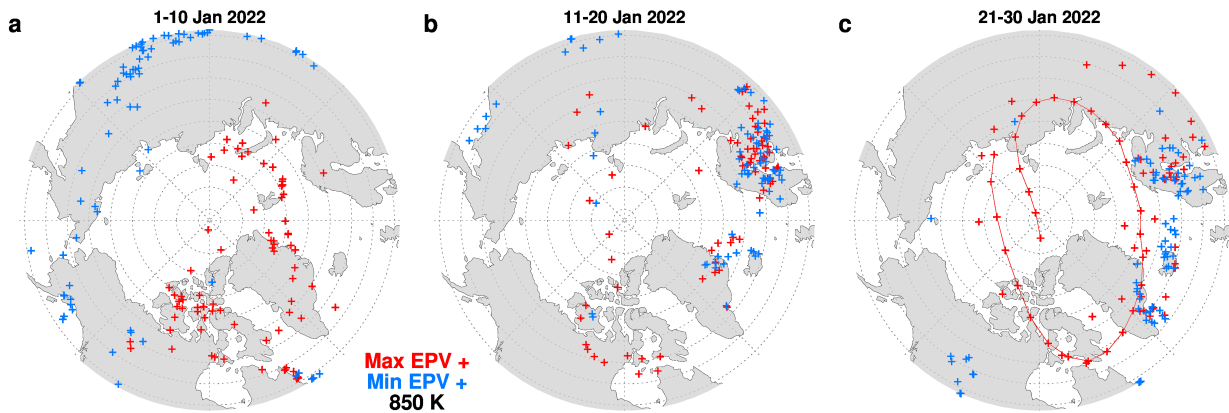
398 Another possible mechanism for the origin of the mesoscale vortices is vortex roll-up
399 (Dritschel and Polvani 1992), a shear instability occurring in some vorticity strips. These are
400 usually seen in EPV filaments well outside of the main polar vortex that are pulled off the polar
401 vortex by breaking planetary waves (McIntyre and Palmer 1983). This differs from the situation
402 in January 2022 where the EPV is split while still aligned with the main vortex flow, however
403 the end result is an isolated strip of EPV and hence, potential shear instability. It is likely that a
404 combination of instability mechanisms is at play during the complex dynamics of January 2022.



405 FIG. 14. a) zonal mean wind averaged over 10–60°E (filled contours), the region of negative \bar{q}_y (shaded), the
 406 850K potential temperature (red contour), the non-dimensional fastest ~~growing~~ growing wave amplitude (blue
 407 contours), and b) EPV (PVU) averaged over 10–60°E as a function of latitude. The box in a) and the shaded
 408 region in b) denotes the stability model domain used

409 4. Summary and Conclusions

410 This study based on the 12 km resolution DAS revealed two new features in the EPV analysis:
 411 high and low fluctuations at the smallest model scale associated with GW breaking, and high values
 412 associated with mesoscale vortices along the edge of the polar vortex. In this case both types of

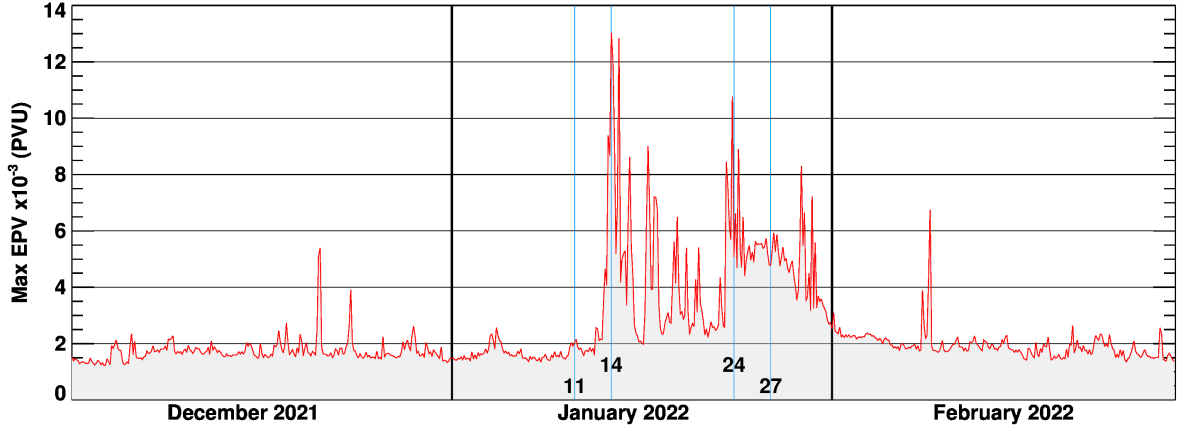


424 FIG. 15. The locations of the maximum (red) and minimum (blue) values of EPV on the 850K potential
 425 temperature surface at each analysis time for a) 1–10, b) 11–20, and c) 21–30 January 2022. The minimum
 426 locations are restricted to the area shown on the map projection. The red curve connects the maximum EPV
 427 locations from 25 January 15 UTC to 29 January 9 UTC.

413 anomalous EPV values were related, as the persistent GW breaking created a region of reversed
 414 EPV gradient that triggered the formation of the mesoscale vortices.

415 The location of NH maximum and minimum values of 850K EPV at each analysis time provides
 416 a convenient overview of the breaking GW regions during January 2022 (Fig. 15). During the
 417 first ten-days the highest EPV values are at the highest latitudes and lowest EPV values are at the
 418 lower latitudes, consistent with the NH climatological poleward gradient of EPV. By the middle of
 419 January, however, the distribution has changed with maximum and minimum EPV locations close
 420 together over Northern Europe, the Greenland coast, and Iceland. These indicate regions of strong
 421 GW breaking as seen in the EPV field. Later in January, these "salt and pepper" patterns continue
 422 with the addition of several days (25–29 January) when the maximum EPV value was associated
 423 with a propagating mesoscale vortex.

428 The maximum value of 850K EPV can ~~characterized~~ characterize the overall NH winter of
 429 2021–22 with a nominal maximum value of just under 2000 PVU for most of the winter season
 430 (Fig. 16). Starting on 14 January, values that are 5× higher appear, coincident with the appearance
 431 of GW breaking. These spikes continue for the remainder of the month with the addition of a
 432 more consistent in time bulge of high EPV, a signature of the persistent mesoscale vortices. These
 433 dramatic events are mostly over by the start of February.



434 FIG. 16. Maximum EPV value on the 850K potential temperature surface as a function of time (10^{-3} PVU).
 435 11, 14, 24, and 27 January 2022 are denoted by blue vertical lines.

436 How realistic are these very high EPV values seen in DAS? It is difficult to be definitive at this
 437 time. The very smallest scale EPV fluctuations, occurring in association with GW breaking, are
 438 likely greatly ~~influence~~ influenced by the limited model resolution. However, higher horizontal res-
 439 olution leads to more sharply defined mesoscale vortices with higher central EPV values (Fig. 13).
 440 Comparison of the evolution of the mesoscale vortices in FP with the lower resolution MERRA-2
 441 EPV fields (Fig. 13) shows that at lower resolution the FP mesoscale vortices can be identified
 442 as a smoothed version of the higher resolution system. If the wind change is approximately the
 443 same across a mesoscale vortex but the doubled horizontal resolution allows for a doubling of the
 444 gradient, then the EPV values can be expected to double as well.

445 ~~The Only one potential mechanism for the~~ creation of the very high mesoscale vortex EPV values
 446 ~~is left for future investigation. In isentropic coordinates the rate of change of the parcel EPV is~~
 447 ~~given by mesoscale vortices was investigated here. Other, perhaps very different, mechanisms are~~
 448 ~~possible. Additionally, the simple linear instability model examined here lacks the ability to follow~~
 449 ~~the perturbation to finite amplitude and to grow the EPV values, a distinctive feature of the vortices~~
 450 ~~that needs explanation. Consider the equation for EPV in isentropic coordinates~~ (Andrews et al.
 451 1987, Equ 3.8.5):

$$\tilde{D}P = (\sigma a \cos \phi)^{-1} [-(X \cos \phi)_\phi + Y_\lambda - Q_\lambda v_\theta + Q_\phi u_\theta \cos \phi] + PQ_\theta - QP_\theta,$$

452 where \tilde{D} is the time derivative following the isentropic flow, P is potential vorticity, σ is the
453 isentropic density, a is the radius of the earth, ϕ is latitude, λ is longitude, θ is potential temperature,
454 X and Y are the latitude and longitude frictional forces, u and v are the velocity components, and
455 Q is the diabatic forcing. Neglecting frictional forces and scaling for quasi-geostrophic motion
456 (Haynes and McIntyre 1987), the equation becomes:

$$\tilde{D}P \approx PQ_{\theta} - QP_{\theta}$$

457 While time averaged diabatic heating terms are typically saved in the DAS output, the quadratic
458 terms are not save so additional output would be useful. In addition, the non-geostrophic terms may
459 contribute to the mesoscale vortices. Along It should be noted that, along with the mesoscale high
460 EPV, some regions of mesoscale low EPV stand out. This is especially noticeable in Fig. 12b, the
461 intermediate resolution experiment, near “B” and “C”, suggesting that isentropic redistribution of
462 EPV is playing a role rather than problematic model numerics in creating the high EPV features
463 and supporting the concept of rearrangement of EPV as part of the development of the mesoscale
464 vortices.

465 The different orientation and scale of EPV fluctuations from the associated GWs needs further
466 investigation. Detailed three dimensional models of GW breaking (Fritts et al. 2009a,b) resolve
467 the small scale, rapid, variability created during the breaking process and the generation of EPV
468 by breaking GWs has been recently modeled by Waite and Richardson (2023). These studies
469 suggest that “spanwise”, that is disturbances along the wavefront, commonly develop, however
470 relating these to global scale EPV is not yet clear. While we have focused on a single NH winter
471 in which planetary wave activity was relatively weak to highlight the GWs and their effects on the
472 polar vortex, it is likely that breaking GWs in the mid to upper stratosphere are fairly common and
473 routinely contribute to mixing at the edge of the polar vortex.

474 In future studies we plan to examine other years when high resolution FP DAS fields are available
475 along with results from test model and assimilation experiments at higher horizontal and vertical
476 resolution. More evaluation of the amount of mixing along the polar vortex edge by the mesoscale
477 vortices is also needed. Even though the scale of these vortices is relatively small, the amount of
478 mixing could be substantial as these mesoscale vortices form where tracer gradients are large. In
479 addition, since some evidence of the mesoscale vortices can be found at low resolution such as

480 in Fig. 13a, it may be possible to develop a climatology of when these events occur by searching
481 the longer time record of the lower resolution MERRA-2 DAS. Such a climatology would provide
482 information of the role played by the mesoscale vortices in observed climatological stratospheric
483 tracer distributions.

484 *Acknowledgments.* ~~his~~This work was supported by NASA MAP (Grant NNG17HP01C) and
485 ACMAP programs (Grants 80NSSC19K1005, NNH18ZDA001N). Support for MJA provided
486 by NASA Grant Nos. 80NSSC23K0519 and 80NSSC23K1311. Resources supporting this work
487 were provided by the NASA High-End Computing (HEC) Program through the NASA Center for
488 Climate Simulation (NCCS) at Goddard Space Flight Center.

489 *Data availability statement.* The GEOS data used in this study/project have been provided by
490 the Global Modeling and Assimilation Office (GMAO) at NASA Goddard Space Flight Cen-
491 ter. The Forward Processing (FP) DAS output are archived at [https://portal.nccs.nasa.](https://portal.nccs.nasa.gov/datashare/gmao/geos-fp/das)
492 [gov/datashare/gmao/geos-fp/das](https://portal.nccs.nasa.gov/datashare/gmao/geos-fp/das) and the system used in this study is labeled f5271_fp.
493 The MERRA-2 data is available from the NASA’s Goddard Earth Sciences Data and In-
494 formation Services Center (GES DISC, <https://disc.gsfc.nasa.gov/datasets?project=MERRA-2>).
495 Specific MERRA-2 data sets used are contained in the references. The AIRS brightness
496 temperatures are available from [https://datapub.fz-juelich.de/slcs/airs/gravity_](https://datapub.fz-juelich.de/slcs/airs/gravity_waves/html/view_2022_014.html)
497 [waves/html/view_2022_014.html](https://datapub.fz-juelich.de/slcs/airs/gravity_waves/html/view_2022_014.html) The IDL (Interactive Data Language) code used for the
498 quasi-geostrophic instability model is archived at [https://gmao.gsfc.nasa.gov/gmaoftp/](https://gmao.gsfc.nasa.gov/gmaoftp/larrycoy/instability_code/stability_package.pro)
499 [larrycoy/instability_code/stability_package.pro](https://gmao.gsfc.nasa.gov/gmaoftp/larrycoy/instability_code/stability_package.pro). The x0048 DAS fields used to
500 construct intermediate resolution EPV fields on 25 and 27 January 2022 are archived at
501 https://gmao.gsfc.nasa.gov/gmaoftp/larrycoy/mesoscale_vortices.

502 **References**

- 503 Achatz, U., and Coauthors, 2024: Atmospheric gravity waves: Processes and parameterization.
504 *Journal of the Atmospheric Sciences*, **81** (2), 237–262, [https://doi.org/10.1175/JAS-D-23-0210.](https://doi.org/10.1175/JAS-D-23-0210.1)
505 1, URL <https://journals.ametsoc.org/view/journals/atsc/81/2/JAS-D-23-0210.1.xml>.
- 506 Albers, J. R., and T. Birner, 2014: Vortex preconditioning due to planetary and gravity
507 waves prior to sudden stratospheric warmings. *Journal of the Atmospheric Sciences*, **71** (11),
508 4028 – 4054, <https://doi.org/10.1175/JAS-D-14-0026.1>, URL [https://journals.ametsoc.org/](https://journals.ametsoc.org/view/journals/atsc/71/11/jas-d-14-0026.1.xml)
509 [view/journals/atsc/71/11/jas-d-14-0026.1.xml](https://journals/ametsoc.org/view/journals/atsc/71/11/jas-d-14-0026.1.xml).
- 510 Alexander, M. J., 2010: Gravity waves in the stratosphere. *The Stratosphere: Dynamics, Transport,*
511 *and Chemistry*, L. M. Polvani, A. H. Sobel, and D. W. Waugh, Eds., American Geophysical

512 Union, Washington, DC, 109–122.

513 Andrews, D. G., J. R. Holton, and C. B. Leovy, 1987: *Middle Atmosphere Dynamics*. Academic
514 Press, 489 pp.

515 Arnold, N. P., W. M. Putman, and S. R. Freitas, 2020: Impact of resolution and parameterized
516 convection on the diurnal cycle of precipitation in a global nonhydrostatic model. *Journal of
517 the Meteorological Society of Japan. Ser. II*, **98 (6)**, 1279–1304, [https://doi.org/10.2151/jmsj.
518 2020-066](https://doi.org/10.2151/jmsj.2020-066).

519 Butchart, N., 2022: The stratosphere: a review of the dynamics and variability. *Weather and
520 Climate Dynamics*, **3 (4)**, 1237–1272, <https://doi.org/10.5194/wcd-3-1237-2022>, URL <https://wcd.copernicus.org/articles/3/1237/2022/>.

522 Dritschel, D. G., and L. M. Polvani, 1992: The roll-up of vorticity strips on the surface of a sphere.
523 *J. Fluid Mech.*, **234**, 47–69.

524 Fritts, D. C., and M. J. Alexander, 2003: Gravity wave dynamics and effects
525 in the middle atmosphere. *Reviews of Geophysics*, **41 (1)**, [https://doi.org/https://doi.
526 org/10.1029/2001RG000106](https://doi.org/https://doi.org/10.1029/2001RG000106), URL [https://agupubs.onlinelibrary.wiley.com/doi/abs/10.1029/
527 2001RG000106](https://agupubs.onlinelibrary.wiley.com/doi/abs/10.1029/2001RG000106), <https://agupubs.onlinelibrary.wiley.com/doi/pdf/10.1029/2001RG000106>.

528 Fritts, D. C., L. Wang, J. Werne, T. Lund, and K. Wan, 2009a: Gravity wave instability dynamics
529 at high reynolds numbers. part i: Wave field evolution at large amplitudes and high frequencies.
530 *Journal of the Atmospheric Sciences*, **66 (5)**, 1126 – 1148, [https://doi.org/https://doi.org/10.1175/
531 2008JAS2726.1](https://doi.org/https://doi.org/10.1175/2008JAS2726.1), URL <https://journals.ametsoc.org/view/journals/atsc/66/5/2008jas2726.1.xml>.

532 Fritts, D. C., L. Wang, J. Werne, T. Lund, and K. Wan, 2009b: Gravity wave instability dynamics at
533 high reynolds numbers. part ii: Turbulence evolution, structure, and anisotropy. *Journal of the At-
534 mospheric Sciences*, **66 (5)**, 1149 – 1171, [https://doi.org/https://doi.org/10.1175/2008JAS2727.
535 1](https://doi.org/https://doi.org/10.1175/2008JAS2727.1), URL <https://journals.ametsoc.org/view/journals/atsc/66/5/2008jas2727.1.xml>.

536 Gelaro, R., and Coauthors, 2017: The Modern-Era Retrospective Analysis for Research and
537 Applications, Version 2 (MERRA-2). *Journal of Climate*, **30 (14)**, 5419–5454, [https://doi.org/
538 10.1175/JCLI-D-16-0758.1](https://doi.org/10.1175/JCLI-D-16-0758.1), URL <https://doi.org/10.1175/JCLI-D-16-0758.1>, [https://doi.org/
539 10.1175/JCLI-D-16-0758.1](https://doi.org/10.1175/JCLI-D-16-0758.1).

540 GMAO, 2015a: Global Modeling and Assimilation Office, inst3 3d asm Nv: MERRA-2 3D Assim-
541 ilated Meteorological Fields 3-hourly (model level, 0.625x0.5L42), version 5.12.4. Greenbelt,
542 MD, USA: Goddard Space Flight Center Distributed Active Archive Center (GSFC DAAC),
543 accessed June 2016, <https://doi.org/10.5067/WWQSXQ8IVFW8>.

544 GMAO, 2015b: Global Modeling and Assimilation Office, instM 3d asm Np: MERRA-2 3D
545 IAU State, Meteorology Monthly Averaged 3-hourly (p-coord, 0.625x0.5L42), version 5.12.4.
546 Greenbelt, MD, USA: Goddard Space Flight Center Distributed Active Archive Center (GSFC
547 DAAC), accessed June 2016, <https://doi.org/10.5067/2E096JV59PK7>.

548 Haynes, P. H., and M. E. McIntyre, 1987: On the evolution of vorticity and po-
549 tential vorticity in the presence of diabatic heating and frictional or other forces.
550 *Journal of Atmospheric Sciences*, **44** (5), 828 – 841, [https://doi.org/https://doi.org/10.](https://doi.org/https://doi.org/10.1175/1520-0469(1987)044<0828:OTEOVA>2.0.CO;2)
551 [1175/1520-0469\(1987\)044<0828:OTEOVA>2.0.CO;2](https://doi.org/https://doi.org/10.1175/1520-0469(1987)044<0828:OTEOVA>2.0.CO;2), URL [https://journals.ametsoc.org/view/](https://journals.ametsoc.org/view/journals/atsc/44/5/1520-0469_1987_044_0828_oteova_2_0_co_2.xml)
552 journals/atsc/44/5/1520-0469_1987_044_0828_oteova_2_0_co_2.xml.

553 Haynes, P. H., and M. E. McIntyre, 1990: On the conservation and impermeability theorems for
554 potential vorticity. *Journal of Atmospheric Sciences*, **47** (16), 2021 – 2031, [https://doi.org/https://](https://doi.org/https://doi.org/10.1175/1520-0469(1990)047<2021:OTCAIT>2.0.CO;2)
555 [doi.org/10.1175/1520-0469\(1990\)047<2021:OTCAIT>2.0.CO;2](https://doi.org/https://doi.org/10.1175/1520-0469(1990)047<2021:OTCAIT>2.0.CO;2), URL [https://journals.ametsoc.](https://journals.ametsoc.org/view/journals/atsc/47/16/1520-0469_1990_047_2021_otcait_2_0_co_2.xml)
556 [org/view/journals/atsc/47/16/1520-0469_1990_047_2021_otcait_2_0_co_2.xml](https://journals/atsc/47/16/1520-0469_1990_047_2021_otcait_2_0_co_2.xml).

557 Hoffmann, L., M. J. Alexander, C. Clerbaux, A. W. Grimsdell, C. I. Meyer, T. Rößler, and
558 B. Tournier, 2014: Intercomparison of stratospheric gravity wave observations with AIRS
559 and IASI. *Atmospheric Measurement Techniques*, **7** (12), 4517–4537, [https://doi.org/10.5194/](https://doi.org/10.5194/amt-7-4517-2014)
560 [amt-7-4517-2014](https://doi.org/10.5194/amt-7-4517-2014), URL <https://amt.copernicus.org/articles/7/4517/2014/>.

561 Holt, L. A., M. J. Alexander, L. Coy, C. Liu, A. Molod, W. Putman, and S. Pawson, 2017: An eval-
562 uation of gravity waves and gravity wave sources in the southern hemisphere in a 7 km global cli-
563 mate simulation. *Quarterly Journal of the Royal Meteorological Society*, **143** (707), 2481–2495,
564 <https://doi.org/https://doi.org/10.1002/qj.3101>, URL [https://rmets.onlinelibrary.wiley.com/doi/](https://rmets.onlinelibrary.wiley.com/doi/abs/10.1002/qj.3101)
565 [abs/10.1002/qj.3101](https://rmets.onlinelibrary.wiley.com/doi/abs/10.1002/qj.3101), <https://rmets.onlinelibrary.wiley.com/doi/pdf/10.1002/qj.3101>.

566 Hoskins, B. J., M. E. McIntyre, and A. W. Robertson, 1985: On the use and significance
567 of isentropic potential vorticity maps. *Quarterly Journal of the Royal Meteorological Soci-*
568 *ety*, **111** (470), 877–946, <https://doi.org/https://doi.org/10.1002/qj.49711147002>, URL <https://doi.org/https://doi.org/10.1002/qj.49711147002>, URL <https://doi.org/https://doi.org/10.1002/qj.49711147002>.

569 //rmets.onlinelibrary.wiley.com/doi/abs/10.1002/qj.49711147002, <https://rmets.onlinelibrary.wiley.com/doi/pdf/10.1002/qj.49711147002>.

571 Matthias, V., and M. Ern, 2018: On the origin of the mesospheric quasi-stationary planetary
572 waves in the unusual arctic winter 2015/2016. *Atmos. Chem. Phys.*, **18**, 4803–4815, URL
573 <https://doi.org/10.5194/acp-18-4803-2018>.

574 McCormack, J. P., L. Coy, and W. Singer, 2014: Intraseasonal and interannual variability
575 of the quasi 2 day wave in the northern hemisphere summer mesosphere. *Journal of Geo-*
576 *physical Research: Atmospheres*, **119** (6), 2928–2946, [https://doi.org/https://doi.org/10.1002/](https://doi.org/https://doi.org/10.1002/2013JD020199)
577 [2013JD020199](https://doi.org/https://doi.org/10.1002/2013JD020199), URL <https://agupubs.onlinelibrary.wiley.com/doi/abs/10.1002/2013JD020199>,
578 <https://agupubs.onlinelibrary.wiley.com/doi/pdf/10.1002/2013JD020199>.

579 McFarlane, N. A., 1987: The effect of orographically excited gravity wave drag on the general
580 circulation of the lower stratosphere and troposphere. *J. Atmos. Sci.*, **44**, 1775–1800.

581 McIntyre, M. E., and T. N. Palmer, 1983: Breaking planetary waves in the stratosphere. *Nature*,
582 **305**, 593–600.

583 Nash, E. R., P. A. Newman, J. E. Rosenfield, and M. R. Schoeberl, 1996: An objective
584 determination of the polar vortex using Ertel’s potential vorticity. *Journal of Geophysi-*
585 *cal Research: Atmospheres*, **101** (D5), 9471–9478, [https://doi.org/https://doi.org/10.1029/](https://doi.org/https://doi.org/10.1029/96JD00066)
586 [96JD00066](https://doi.org/https://doi.org/10.1029/96JD00066), URL <https://agupubs.onlinelibrary.wiley.com/doi/abs/10.1029/96JD00066>, <https://agupubs.onlinelibrary.wiley.com/doi/pdf/10.1029/96JD00066>.

588 Okui, H., C. J. Wright, N. P. Hindley, E. J. Lear, and K. Sato, 2023: A comparison of stratospheric
589 gravity waves in a high-resolution general circulation model with 3-d satellite observations.
590 *Journal of Geophysical Research: Atmospheres*, **128** (13), e2023JD038795, [https://doi.org/](https://doi.org/https://doi.org/10.1029/2023JD038795)
591 [https://doi.org/10.1029/2023JD038795](https://doi.org/https://doi.org/10.1029/2023JD038795), URL [https://agupubs.onlinelibrary.wiley.com/doi/abs/](https://agupubs.onlinelibrary.wiley.com/doi/abs/10.1029/2023JD038795)
592 [10.1029/2023JD038795](https://agupubs.onlinelibrary.wiley.com/doi/abs/10.1029/2023JD038795), e2023JD038795 2023JD038795, <https://agupubs.onlinelibrary.wiley.com/doi/pdf/10.1029/2023JD038795>.

594 Putman, W. M., and S.-J. Lin, 2007: Finite-volume transport on various cubed-sphere grids.
595 *Journal of Computational Physics*, **227** (1), 55–78, [https://doi.org/https://doi.org/10.1016/j.jcp.](https://doi.org/https://doi.org/10.1016/j.jcp.2007.07.022)
596 [2007.07.022](https://doi.org/https://doi.org/10.1016/j.jcp.2007.07.022), URL <https://www.sciencedirect.com/science/article/pii/S0021999107003105>.

597 Sato, K., R. Yasui, and Y. Miyoshi, 2018: The momentum budget in the stratosphere, mesosphere,
598 and lower thermosphere. Part I: Contributions of different wave types and in situ generation of
599 Rossby waves. *J. Atmos. Sci.*, **75**, 3613–3633, URL <https://doi.org/10.1175/JAS-D-17-0336.1>.

600 Shibuya, R., and K. Sato, 2019: A study of the dynamical characteristics of inertia–gravity
601 waves in the antarctic mesosphere combining the PANSY radar and a non-hydrostatic general
602 circulation model. *Atmospheric Chemistry and Physics*, **19** (5), 3395–3415, <https://doi.org/10.5194/acp-19-3395-2019>, URL <https://acp.copernicus.org/articles/19/3395/2019/>.

604 Siskind, D. E., S. D. Eckermann, J. P. McCormack, L. Coy, K. W. Hoppel, and N. L. Baker, 2010:
605 Case studies of the mesospheric response to recent minor, major, and extended stratospheric
606 warmings. *J. Geophys. Res.*, **115** (D00N03), <https://doi.org/doi:10.1029/2010JD014114>.

607 Smith, A. K., 1996: Longitudinal variations in mesospheric winds: Evidence for gravity wave
608 filtering by planetary waves. *J. Atmos. Sci.*, **53** (8), 1156–1173.

609 Stevens, B., and Coauthors, 2019: DYAMOND: the DYnamics of the Atmospheric general
610 circulation Modeled On Non-hydrostatic Domains. *Prog Earth Planet Sci*, **6** (61), URL
611 <https://doi.org/10.1186/s40645-019-0304-z>.

612 Waite, M. L., and N. Richardson, 2023: Potential vorticity generation in breaking gravity
613 waves. *Atmosphere*, **14** (5), <https://doi.org/10.3390/atmos14050881>, URL <https://www.mdpi.com/2073-4433/14/5/881>.

615 Watanabe, S., and S. Miyahara, 2009: Quantification of the gravity wave forcing of the mi-
616 grating diurnal tide in a gravity wave–resolving general circulation model. *J. Geophys. Res.*,
617 **114** (D07110), doi:10.1029/2008JD011218.

618 Zhu, Y., R. Todling, and N. Arnold, 2022: Observation impact and information retention in
619 the lower troposphere of the gmao geos data assimilation system. *Monthly Weather Review*,
620 **150** (8), 2187 – 2205, <https://doi.org/https://doi.org/10.1175/MWR-D-21-0334.1>, URL <https://journals.ametsoc.org/view/journals/mwre/150/8/MWR-D-21-0334.1.xml>.

621